Determination and analysis of long-wavelength transition zone structure using *SS* precursors

C. Houser,[1],*[†] G. Masters,[1] M. Flanagan[2] and P. Shearer[1]

[1]*Institute of Geophysics and Planetary Physics, University of California San Diego, La Jolla, CA 92093, USA. E-mail: creif@pmc.ucsc.edu*
[2]*Lawrence Livermore National Laboratory,* PO Box 808, L-205, *Livermore, CA 94551, USA*

GJI Seismology

SUMMARY
Global mapping of 410 and 660 km discontinuity topography and transition zone thickness has proven to be a powerful tool for constraining mantle chemistry, dynamics and mineralogy. Numerous seismic and mineral physics studies suggest that the 410 km discontinuity results from the phase change of olivine to wadsleyite and the 660 km discontinuity results from the phase change of ringwoodite to perovskite and magnesiowustite. Underside reflections of the 410 and 660 km discontinuities arrive as precursors to *SS*. With the recent development of a semi-automated method of determining *SS* arrivals, we have more than tripled the Flanagan and Shearer (1998a) data set of handpicked *SS* waveforms. We are able to increase resolution by stacking waveforms in 5° rather than 10° radius bins as well as increasing data coverage significantly in the southern hemisphere. The resulting *SS-S410S* and *SS-S660S* times are heavily influenced by upper-mantle velocity structure. We perform a joint inversion for discontinuity topography and velocity heterogeneity as well as performing a simple velocity correction to the precursor differential times and find little difference between the two methods. The 660 km discontinuity topography and transition zone thickness are correlated with velocities in the transition zone whereas the 410 km discontinuity topography is not. In addition, the 410 km discontinuity topography is not correlated with the 660 km discontinuity topography, rather anticorrelated, as expected due to the opposite signs of the Clapeyron slopes of their respective phase changes. These results suggest that, whereas the topography of 660 km discontinuity could be dominated by thermal effects, the topography of the 410 km discontinuity is likely dominated by compositional effects. In addition, unlike previous studies which find less topography on the 410 km discontinuity than on the 660 km discontinuity, our 410 and 660 km topography have similar amplitudes.

Key words: Phase transitions; Body waves.

1 INTRODUCTION

Within the mantle, the largest velocity jumps occur at approximate depths of 410 and 660 km and are thus referred to as the 410 and the 660 km discontinuity, respectively. The region between these two discontinuities is characterized by high velocity gradients that are steeper than expected from the compressional effects of pressure. However, the region below the 660 km discontinuity (actually below about 800 km) extending down to a few hundred kilometres above the core–mantle boundary is characterized by smooth velocity gradients, as expected for adiabatic increases in temperature and pressure within the mantle. In contrast, the mantle above the discontinuities is also characterized by high velocity gradients. The region between the upper and lower mantle, which is bounded by the 410 and 660 km discontinuities, is termed the 'transition zone', and its width varies with structure along these discontinuities.

The shear impedance contrasts across the 410 and 660 km discontinuities are small, around 4 and 8 per cent, respectively, for PREM (Dziewonski & Anderson 1981), but can range from 6 to 12 and 7 to 13 per cent (Shearer & Flanagan 1999). As a result, reflected phases from these discontinuities are small in amplitude and require the stacking of multiple records to amplify their signal above the noise level of most seismograms.

Most studies of the transition zone use the *Pds* phases, an upgoing *P* wave converted to an *S* wave where *d* refers to the conversion depth. These so-called 'receiver function' analyses (Langston 1979) essentially measure the lapse time between the initial *P* arrival and the converted *S* arrival to detect discontinuity depth and likewise, transition zone thickness. The technique deconvolves the vertical component *P* phase from the radial component *SV* phase

to enhance and normalize the signal of the converted phase before stacking (Vinnik 1977; Vinnik *et al.* 1983; Paulssen 1985, 1988; Kind & Vinnik 1988; Amnon 1991; Shearer 1991; Stammler *et al.* 1991; Chen *et al.* 1997; Gurrola & Minster 1998; Shen *et al.* 1998). Receiver functions have resolution on scales of hundreds of kilometres, but only in the vicinity of multicomponent seismic stations.

Some receiver function studies have combined data arriving from all azimuths to determine an average transition zone thickness underneath stations on a continental scale (Bostock 1996; Vinnik *et al.* 1996; Ramesh *et al.* 2002; Lebedev *et al.* 2003) or on a global scale (Chevrot *et al.* 1999; Lawrence & Shearer 2006a). These studies have the ability to detect large-scale patterns in discontinuity topography. The Bostock (1996) and Ramesh *et al.* (2002) studies find that transition zone thickness is close to the global average for most of the North American continent, except for the tectonically active western regions where the thickness can vary by up to 10 km. According to Vinnik *et al.* (1996), the transition zone beneath Eurasia is consistently thicker than average with no thickening due to the presence of the subducting slab to the east. Lebedev *et al.* (2003) find that the transition zone thickness variations correlate with seismic velocity beneath Australia. Chevrot *et al.* (1999) and Lawrence & Shearer (2006a) also find a positive but small correlation between transition zone thickness and upper-mantle shear velocity.

Other receiver function studies concentrate on specific tectonic environments and often map topography as a function of azimuth around a station. The phase transitions that likely lead to the 410 and 660 km discontinuities (discussed in detail below) should change depth in the presence of a thermal anomaly. To test the notion that the transition zone should thin in warm regions and thicken in cold regions, many authors focus on hotspots and subduction zones. Hotspot studies (Shen *et al.* 1998; Li *et al.* 2000a, 2003; Owens *et al.* 2000; Hooft *et al.* 2003) generally find that the transition zone thins beneath hotspots as expected. Likewise, subduction zone studies (Li *et al.* 2000b; Lebedev *et al.* 2002; Saita *et al.* 2002; Ai *et al.* 2003; Ramesh *et al.* 2005; Tonegawa *et al.* 2005; van der Meijde *et al.* 2005) find that the transition zone thickens in these cold regions, while (Ai *et al.* 2005) shows a thinning under central Alaska. Other areas that are well sampled by receiver functions include western North America (Dueker & Sheehan 1997, 1998; Gilbert *et al.* 2003) and southern Africa (Gao *et al.* 2002; Stankiewicz *et al.* 2002; Blum & Shen 2004; Niu *et al.* 2004). The western North America studies show that the 410 and 660 km discontinuities are not necessarily correlated to surface tectonics or anticorrelated with each other. However, the studies in the southern Africa Kappaval craton demonstrate that the thermal or chemical influence of the continental keel may extend deep enough to affect the 410 km discontinuity.

Deep earthquakes that occur within the transition zone create reflected and converted phases from the discontinuities near the source. Using the converted phase *S660P*, the depth of the 660 km discontinuity in subduction zones has been found to be depressed anywhere from 20 to 60 km (Richards & Wicks 1990; Wicks & Richards 1993; Niu & Kawakatsu 1995; Collier & Helffrich 1997; Castle & Creager 1998). Correspondingly, the reflected phases from subduction zone earthquakes, *p410P*, *s410P* and *s410S*, indicate that the 410 km discontinuity shallows by 10–60 km (Vidale & Benz 1992; Zhang & Lay 1993; Ritsema *et al.* 1995; Collier & Helffrich 1997; Flanagan & Shearer 1998b). These findings are consistent with the majority of receiver function studies that indicate the 410 and 660 km discontinuities shallow and deepen, respectively, due to the cold thermal anomaly of the subducting slab, resulting in anticorrelated topography. However, a recent study by Tibi & Wiens (2005) found a depressed 410 km discontinuity in the region of the

subducting Tonga slab using a variety of the reflected and converted phases recorded by the Seismic Arrays in Fiji and Tonga (SAFT) experiment. The finding of a depressed 410 km discontinuity suggests that the olivine to wadsleyite phase change is sensitive to factors other than just the thermal anomaly in this region.

In the early 1990s, the data compiled from the global seismic network had become numerous and extensive enough to begin global mapping of 410 and 660 km discontinuity topography. Revenaugh & Jordan (1991) used *ScS* reverberations to determine 410 and 660 km discontinuity depth and topography. They found peak-to-peak topography on the discontinuities to be no more than 25 km for wavelengths of 500–5000 km. Shearer (1991) used stacks of long-period records, plotted as a function of source-receiver distance, to determine topography on the 410 and 660 km discontinuities. The study found peak-to-peak topography of 5 km on the 410 km discontinuity and 10 km on the 660 km discontinuity from the global stacks, but regional stacks showed topography that varied by as much as 20 km.

Underside reflections of *SS* off the 410 and 660 km discontinuities arrive as precursors to *SS*, Fig. 1. To date, *SS* precursors are the main type of data providing global coverage of both the 410 and 660 km discontinuities. However, they can resolve only the long wavelength features (thousands of kilometres) of the discontinuities due to the broad sensitivity of the Fresnel zone at their bounce point. Initial *SS* precursor studies found 30 km peak-to-peak topography on the 410 and 660 km discontinuities (Shearer & Masters 1992; Shearer 1993). These analyses were later expanded upon with vastly more data for *SS* precursors (Flanagan & Shearer 1998a) and *PP* precursors (Flanagan & Shearer 1999). Peak-to-peak topography of around 30 km was observed on the 660 km discontinuity and 20 km on the 410 km discontinuity. Gu *et al.* (1998) also mapped global 410 and 660 km discontinuity topography with *SS* precursors with similar findings. Recently, Chambers *et al.* (2005) used *P410P* and *S410S* to produce individual and joint maps of global 410 km discontinuity topography with features that differ from the previous *SS* precursor studies (discussed in detail below). To date the consensus of studies which measure topography of the 410 and 660 km discontinuities is that the transition zone is a global feature with relatively small changes (around 20 km) in depth from the average (Shearer 2000).

Here we seek to improve the global mapping of the discontinuities by employing a recent semi-automated method for determining *SS* phase arrivals. Using the cluster analysis method described in Houser *et al.* (2008), we have quickly determined the arrival times of more than 28 000 *SS* arrivals. First we investigate the effect of adding our absolute *SS* arrival measurements to the Flanagan & Shearer (1998a) *SS* measurements. The combined data set is over three times the size of the original, providing better coverage in previously poorly constrained regions (mostly in the southern hemisphere). Fig. 2 (top panel) shows the number of *SS* precursors that fall within 5° radius bins for the new combined data set (over 39 800 measurements) and Fig. 2 (bottom panel) is the number from the Flanagan & Shearer (1998a) study (around 13 000 measurements). The increased coverage of the expanded data set allows us to be more confident in observed topography in many areas of the southern hemisphere. The increased coverage also allow for more accurate interpretations of the relative behaviour of the 410 and 660 km discontinuity topography and transition zone thickness.

Next, we investigate the effects of velocity anomalies on the *SS*–*SdS* times (where *d* stands for the 410 or 660 km discontinuity). Past precursor and receiver function studies of discontinuity topography assume a mantle velocity model and map the traveltime anomalies as changes in topography. Likewise, typical tomography studies
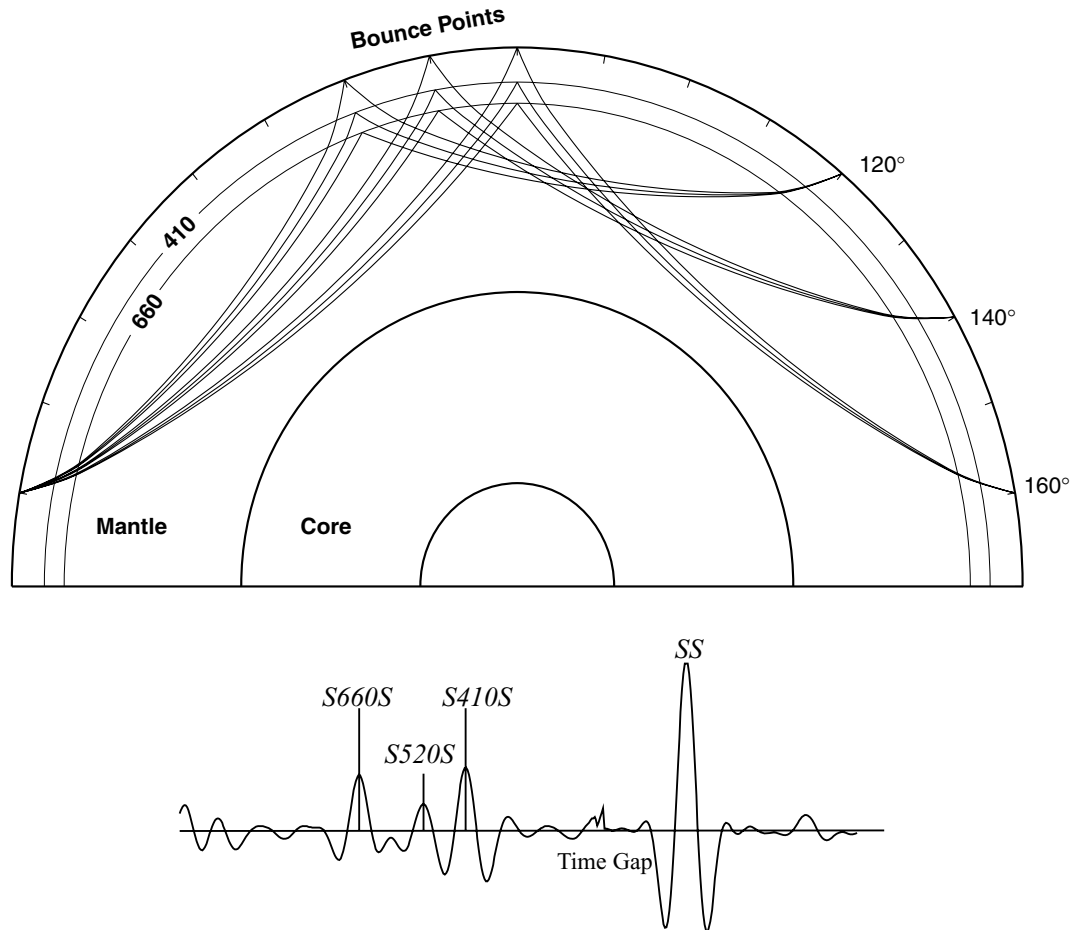
Figure 1. Top panel: Ray geometry of *SS* precursors (adapted from Flanagan & Shearer (1998a)). Bottom panel: Actual precursor stack used in this study from the NW Pacific including 445 seismograms. There is a time gap between the main *SS* arrival and the precursors.

parametrize the Earth as spherical shells and map the traveltime anomalies as changes in velocity within each shell. Most previous mappings of the 410 and 660 km discontinuities have neglected the trade-off between the choice of velocity model and boundary depth on the traveltimes. The exception is a study by Gu *et al.* (2003) which is discussed below. Our inversion method uses a variety of body wave, surface wave and *SS–SdS* data to simultaneously invert for mantle shear velocity anomalies and 410 and 660 km discontinuity topography. We compare the discontinuity topography from this joint inversion with the topography derived by correcting the precursor times for a known velocity model to determine which method is preferable for removing the effects of upper-mantle structure.

In the last part of the paper, we analyse the results to understand the origin of the topography. We compare the 410 and 660 km discontinuity topography with each other and with the velocities within the transition zone. We also compare the transition zone thickness to the velocity structure. We find that the 660 km discontinuity topography and thus transition zone thickness is dominated by the thermal structure of subducting slabs. However, in many regions the 410 km discontinuity topography does not correspond to our understanding of the thermal and chemical state of the mantle transition zone.

2 *SS* PRECURSOR MEASUREMENTS

The *SS* measurements of Flanagan & Shearer (1998a) (henceforth referred to as F&S) were determined manually by selecting the max-

imum of the *SS* pulse from seismograms recorded by the Incorporated Research Institutions for Seismology (IRIS), Global Seismic Network (GSN) and Geoscope between 1976 and the end of 1995. They used the transverse component filtered to the old SRO network response to produce long-period seismograms. The data were restricted to earthquakes at depths shallower than 75 km and distances of 110–180° to avoid interference with depth phases and topside reflections. The cluster analysis technique measures the onset of the *SS* arrival. To make our data compatible with the F&S times, we perform an automated search for the maximum of the *SS* pulse within 40 s of the onset time.

Our cluster analysis *SS* data were measured from the beginning of 1995. Before the late 1990s, there were not enough traces for each event with high signal-to-noise ratios to properly apply cluster analysis. Consequently, our data set is a natural extension of the previous F&S handpicked *SS* data set, with enough overlap to directly compare our methods. Comparing the overlapping measurements for 1995, our *SS* peak times are within a few tenths of a second of the F&S times. Around 13 500 manual *SS* times were used in the F&S study. The cluster analysis data set of *SS* arrival times is based on events with $m_b > 5.5$ from all global networks and available PASSCAL deployments for the years 1995–2005. The seismograms used in the cluster analysis are also filtered to the response of station SRO to be compatible with earlier data. The details of the cluster analysis method do not influence the differential *SS-SdS* times measured here. Rather the cluster analysis simply provides a means to

Data Coverage

SS Bounce Points, This Study
Total = 39,815

Number in Cap

SS Bounce Points, F&S 1998a
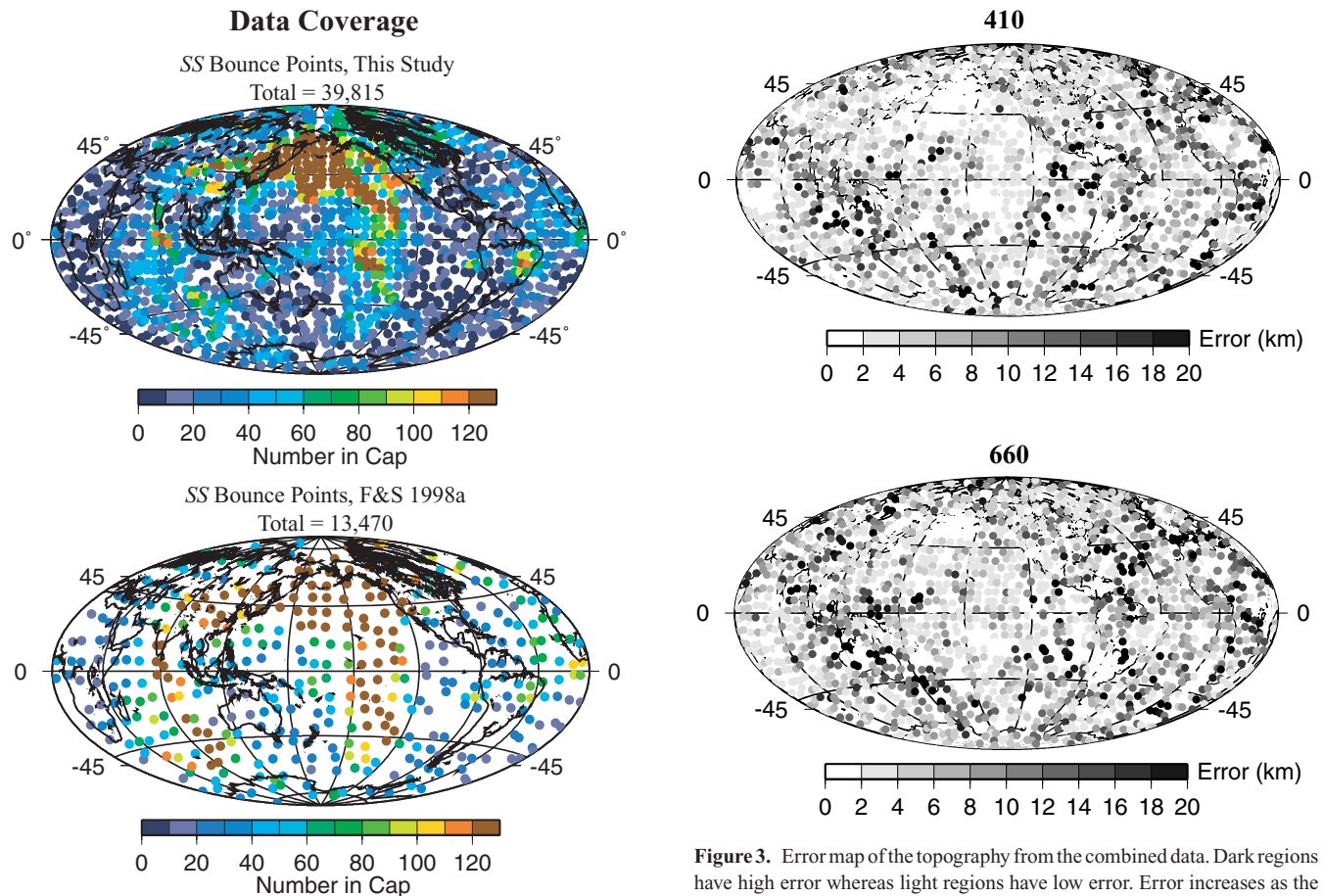#### Total = 13,470

Number in Cap

Figure 2. Top panel: Five degree radius bins used for stacking *SS* precursors in this study. Bins with less than 6 measurements are not plotted. Bottom panel: Ten degree radius bins used for stacking *SS* precursors in the Flanagan and Shearer (1998a) study. The bins are shaded according to the number of *SS* rays with surface bounce points within each bin.

assemble a catalogue of waveforms with high-quality *SS* phases. With the addition of these cluster analysis *SS* times, the number of measurements grows to over 39 800 *SS* times.

The traces with identified *SS* phases are stacked using the method of Flanagan & Shearer (1998a) which is summarized here. The world is subdivided into 5° radius circular caps with centres that are separated by approximately 5°. Due to the increased size of our combined data set, we are able to decrease the stacking cap size from 10° used in F&S. The cap locations and the number of traces with bounce points within each cap are shown in Fig. 2. Traces with bounce points that fall within a cap are deconvolved using simple spectral division of the *SS* pulse and acausal filtering to reduce side lobes. The deconvolved traces are then stacked along the predicted traveltime curve for *S410S* and again for *S660S* using PREM (Dziewonski and Anderson 1981) evaluated at a period of 20 s. This differs from F&S who used the intermediate curve for *S550S*; however, the difference is very small. Like F&S, we also use a reference distance of 138° for stacking. The *SS*–*SdS* time is the difference of the peak of the *SS* pulse and the maximum of the stacked trace in a time window for the expected arrival times of *S660S* (starting 233 s before *SS*) and *S410S* (starting 161 s before *SS*).

A boot-strap random resampling technique is applied to the traces in each cap to determine the error on the *SS*–*SdS* times. The cap

410

Error (km)

660

Error (km)

Figure 3. Error map of the topography from the combined data. Dark regions have high error whereas light regions have low error. Error increases as the number of traces in the stack decreases (see Fig. 2).

locations shown in Fig. 2 are adjusted to reflect the actual average bounce point location of the traces that fall within the cap. Caps with less than six traces in their stack are not used in any further analysis and, therefore, are excluded from Fig. 2 (top panel). F&S exclude caps with less than 10 traces in their study, so these caps are not included in Fig. 2 (bottom panel). The updated data set reinforces coverage in many areas while also filling in many of the pre-existing holes in the Indian Ocean, Atlantic Ocean and southern hemisphere in general. Gaps in coverage exist on the western side of South America and Africa. In the well-covered region in the northwest Pacific Ocean, the number of seismograms contributing to a stacked trace now exceeds 200. The actual stacked traces from each cap are available on the corresponding author's website.

Even though we have improved the coverage and increased the number of traces in each cap by combining the cluster analysis *SS* data set with the F&S *SS* data set, caps with high error remain. Fig. 3 shows the depth error in this study for 410 (top panel) and 660 (bottom panel) km discontinuity topography. The error is calculated by converting the time errors from the boot-strap random resampling to depth errors. Regions with large error are dark grey while those with low error are white. For most of the globe, the error on the topography for both discontinuities is less than 3 km. The high error regions occur where the *SS* precursors have very low amplitude in the stacked traces. A few studies have suggested that precursor measurements may not accurately represent topography due to the effects of topography of smaller dimension than the first Fresnel zone of *SS* (Chaljub & Tarantolla 1997; Neele *et al.* 1997) or the off-path effects not accounted for by ray theory (Zhao & Chevrot

2003). However, Shearer *et al.* (1999) has shown that the precursor measurements are robust.

The deviation from the average for the transition zone width (top panel), 410 (middle panel) and 660 (bottom panel) km discontinuity topography from the combined *SS* data set is shown in Fig. 4. The *SS–SdS* times are converted to depths from predicted traveltimes for precursor arrivals using PREM (Dziewonski & Anderson 1981) and have been corrected for the global crustal model CRUST 2.0 of
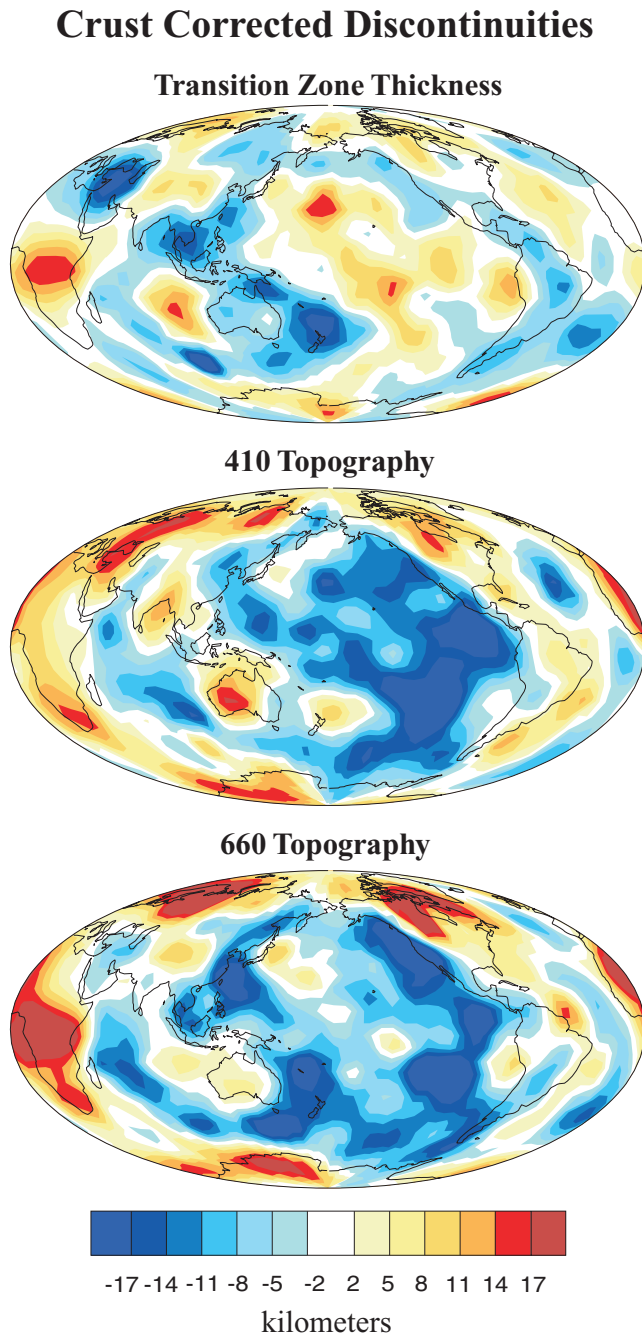
Crust Corrected Discontinuities

Transition Zone Thickness

410 Topography

660 Topography

Figure 4. The transition zone thickness (top panel) and 410 (middle panel) and 660 (bottom panel) km discontinuity topography. The depths are deviations from the mean, corrected for CRUST 2.0 and smoothed to spherical harmonic degree 20. The average depths of the 410 and 660 km discontinuities are 410 and 650 km, respectively, resulting in an average transition zone thickness of 240 km using 20 s PREM.

Laske *et al.* (http://mahi.ucsd.edu/Gabi/rem.dir/crust/crust2.html). Spherical splines are computed from the cap measurements and interpolated at a regular interval of 5° in longitude and latitude. The splines minimize the squared Laplacian integrated over the sphere and thus smooth out short wavelength (high harmonic degree) structure (Parker 1994). Fitting our data to χ^2/N of 0.5 results in a model that is the equivalent to a spherical harmonic truncation at about degree 20. All of the following maps based on the *SS* precursor data are constructed in this fashion. Negative values (blue) indicate that the discontinuity is deeper than average and likewise positive values (red) indicate that it is shallower than average. The transition zone thickness is our most robust measurement as it is independent of upper-mantle structure. The transition zone is thickest (blue) in the western Pacific associated with current subduction zones and thinnest (red) under Africa as well as the mid-Atlantic and eastern Indian oceans. The apparent correlation of the 410 and 660 km discontinuity topography is not representative of true structure since both the 410 and 660 km topographies are clearly influenced by upper-mantle velocities. Therefore, before discussing the structure further, it is necessary to determine the best method for removing the effects of upper-mantle velocity heterogeneity.

3 REMOVING THE EFFECTS OF THE UPPER MANTLE ON *SS* PRECURSORS

3.1 Joint inversion for discontinuity topography and velocity anomalies

The inversion method used here is the same as that described in Houser *et al.* (2008) except that the block size is larger. The velocity model is parametrized as equal area blocks measuring 6° at the equator for 18 layers (approximately 100 km thickness in the upper mantle, 200 km thickness in the lower mantle) as well as 6° pixels for the 410 and 660 km discontinuity topography, resulting in 22 920 model parameters. Our block parametrization is equivalent to a spherical harmonic expansion to degree 30. Although our traveltime data sets can resolve features on finer scales, as in Houser *et al.* (2008), we use a block size that is comparable to the broad sensitivities of the precursors at their bounce points. The power in the topography is dominated by structure in the low-order harmonic degrees, so this parametrization is appropriate.

Our inversion uses a combination of surface waves to constrain upper-mantle structure, numerous long-period *S* body wave data and our combined *SS–SdS* times. We use global phase velocity maps of Love (Bassin *et al.* 2000) and Rayleigh (Laske 2004, personal communication) waves at frequencies of 4–15 mHz to constrain upper-mantle velocity structure. The low frequency surface wave data have comparable sensitivities to velocity perturbations and to discontinuity depth. Thus, if inverted alone, surface waves have large trade-offs between velocity anomalies and discontinuity topography. However, the addition of the *SS–SdS* times completely removes this trade-off and allows topography to be recovered. For the inversion, we convert the crust-corrected 410 and 660 km discontinuity depths as well as the transition zone thickness to one-way vertical traveltimes using 20 s PREM (Dziewonski & Anderson 1981).

The body wave data consist of the long-period direct and differential arrival times. Houser *et al.* (2008) describe the cluster analysis technique used to determine the traveltimes of *S* and *SS*. The differential traveltimes, *SS–S* and *ScS–S* were determined with the method of Woodward & Masters (1991a,b) updated in 1999 and 2004, respectively. The sizes of each data set are listed in Table 1.

Table 1. Data sets.

Data type	Start	End	Number of data
S	1976	2005	169 832
P	1976	2005	182 724
SS	1995	2005	28 194
PP	1995	2005	42 710
SS–S	1976	1999	27 560
PP–P	1976	1999	22 595
ScS–S	1976	2005	26 840
Love waves	1989	1999	14 000
Rayleigh waves	1989	1999	42 000

The combination of the body and surface wave data sets provides good coverage throughout most of the mantle. We use the formula given by Dziewonski & Gilbert (1976) relating boundary perturbations to traveltime perturbations

$$\delta t = \frac{-\sqrt{\eta^2 - p^2}^+_-}{r}, \tag{1}$$

$$\eta^+ = \frac{r}{v_+}, \tag{2}$$

$$\eta^- = \frac{r}{v_-}, \tag{3}$$

where t is the traveltime, r is the radius, p is the ray parameter and v is velocity. However, for transmitted rays, the boundary perturbations have negligible contribution to the traveltime perturbations when compared with the velocity perturbations along the ray path.

Similar to the inversion in Houser *et al.* (2008), source mislocation effects are removed using a projection operator, **P** (Masters *et al.* 1996), and we use the LSQR method (Paige & Saunders 1973) to iteratively invert for the velocity perturbations $\delta v/v$, but here we also invert for boundary perturbations $\delta r/r$, where r is the radius of the earth. The vector of time residuals, δt, is divided by their error, e, and denoted as δt_e. The errors on the traveltime residuals are assigned based on the scaled median absolute deviation of δt after the signal from 3-D structure has been removed. The errors on the precursor residuals are assigned based on the boot-strap random resampling of the data. The system to solve is

$$\begin{bmatrix} \frac{\delta v}{v} \\ \dots \\ \frac{\delta r}{r} \end{bmatrix} = \begin{bmatrix} \mathbf{P} \times \mathbf{A} \\ \lambda_1 \mathbf{D}_R \\ \lambda_2 \mathbf{D}_L \\ \lambda_3 \mathbf{D}_L \\ \lambda_4 \mathbf{D}_L \end{bmatrix}^{-1} \times \begin{bmatrix} \mathbf{P} \times \delta t_e \\ 0 \\ 0 \\ 0 \\ 0 \end{bmatrix}, \tag{4}$$

where **A** is the matrix of ray path sensitivities in each block of the model and radial (λ_1), lateral (λ_2), 660 lateral (λ_3) and 410 lateral (λ_4) smoothing parameters are applied to a radial $\mathbf{D}_R$ or lateral $\mathbf{D}_L$ first difference operator. Although we have more data than model parameters, the ray geometry leaves some areas of the model poorly constrained. To have a well-conditioned matrix for the inversion, the smoothing parameters are chosen such that further roughening of the model does not provide an improved fit to the data. The resulting joint model has a variance reduction of 71, 79 and 78 per cent for the 410 km, 660 km and transition zone precursor times, respectively, as well as fitting them to $\chi^2/N = 0.9$.

3.2 Direct velocity correction

The standard method for removing the effects of the upper mantle on the *SS–SdS* times is to correct for a known 3-D velocity model. The traveltime advance or delay along the differential *SS–SdS* ray path is calculated by integrating the 3-D anomalies along the (1-D) ray paths and is then subtracted from the observed *SS–SdS* time. Velocity anomalies are very high in the upper mantle and have a significant effect on the *SS–SdS* times as evidenced by the reflection of surface tectonics such as ocean ridges and cratons in the 410 and 660 km discontinuity topography, Fig. 4. The long wavelength features in shear velocity models are now in quite good agreement (Romanowicz 2003), so the velocity correction should not change significantly due to the choice of shear velocity model. Here we use a 6° shear velocity model from an inversion of the data sets described above that does not include the discontinuities. This model is almost identical to the velocity model obtained by jointly inverting for velocities and topography.

4 RESULTS

To test the amplitude and pattern recovery of the joint inversion, we performed checkerboard tests. A checkerboard pattern is set for a given layer and synthetic data are computed. These synthetic data are then inverted using the same smoothing parameters as for the real data. If the model had perfect resolution, the output model would be the same as the input checkerboard. However, this is never the case in global tomography. Figs 5(a)–(d) shows the results for the 410 km discontinuity topography, 660 km discontinuity topography and the transition zone velocity anomalies for a checkerboard in the velocity model at the layer above 660 km. Figs 5(e)–(h) shows the results for an initial checkerboard of topography on the 660 km discontinuity. The topography does not leak into the velocity model and likewise the velocities do not leak into the topography model. Therefore, there is almost no covariance in velocity and topography model parameters. The deviations to the average transition zone width along with the topography on the 410 and 660 km discontinuities from our joint inversion are shown in Fig. 6. Negative values (blue) indicate that the transition zone is thicker than average or that topography is low. Positive values (red) indicate that the transition zone is thinner than average or that topography is high. The thickest region of transition zone extends from southwest to southeast Asia and continues along the Java trench to New Zealand. This thickening is due to a depression of the 660 km discontinuity accompanied by a rise in the 410 km discontinuity. The transition zone is thin under most of the Pacific due to a depression of the 410 km discontinuity.

The deviations to the average transition zone width along with the topography on the 410 and 660 km discontinuities for the velocity-corrected times are shown in Fig. 7. The results are similar to those from the joint inversion, though are smoother. This is because the joint inversion uses a first-difference smoother while the splining used to make Fig. 7 employs a second derivative smoother. Fig. 8 shows the correlation (left-hand panel) and amplitude (right-hand panel) as a function of harmonic degree for the 410 km discontinuity topography (top panel), 660 km discontinuity topography (middle panel) and transition zone thickness (bottom panel) models from both methods. The maps are highly correlated at all harmonic degrees but the amplitudes of the velocity-corrected maps are larger at long wavelengths, reflecting the difference in the smoothers. Gu *et al.* (2003) also performed a joint inversion for velocities and topography with surface wave, body wave and *SS* precursor data. Their results indicate that there is not a great difference between the
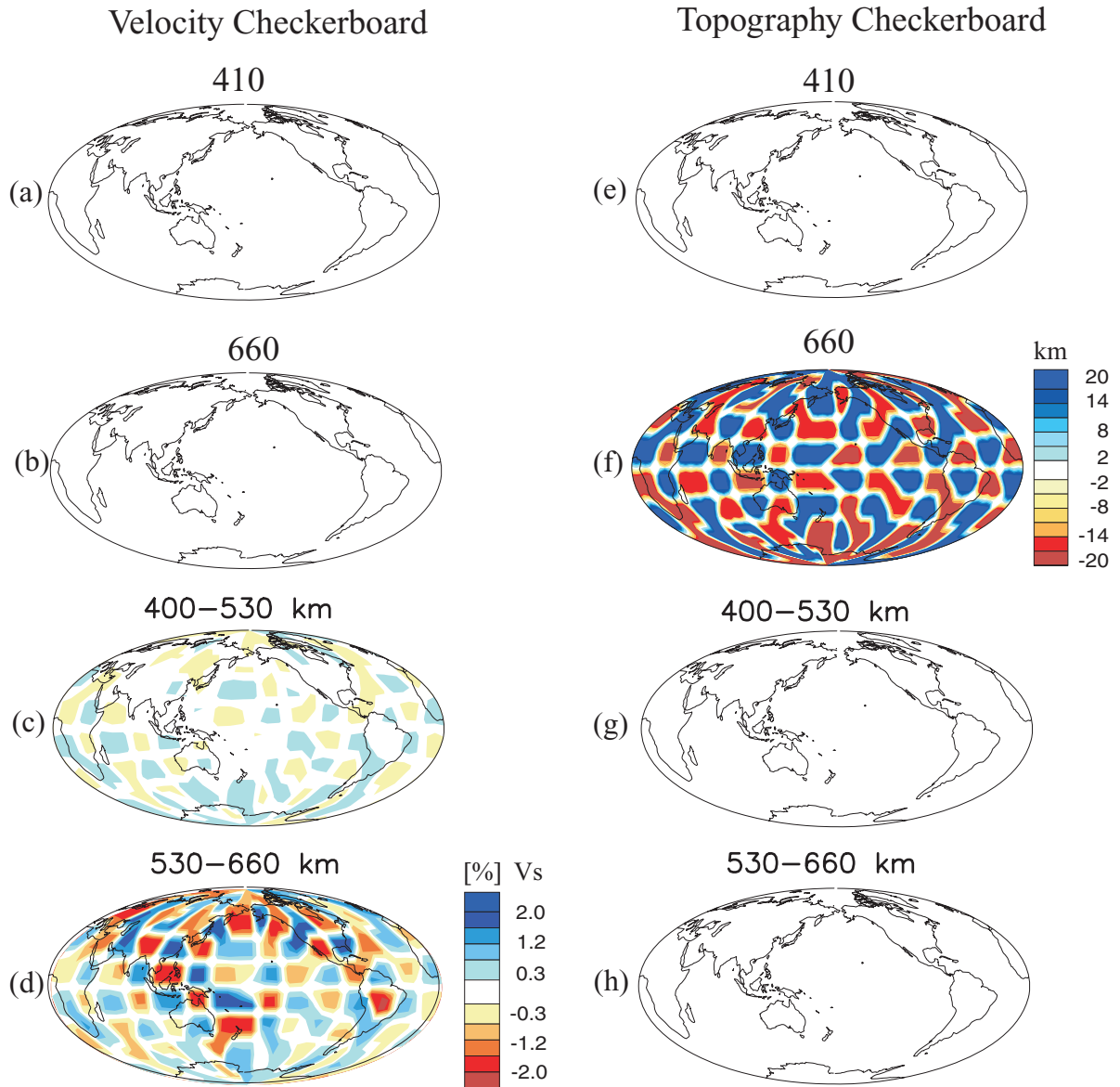
Velocity Checkerboard

410

(a)

660

(b)

400−530 km

(c)

530−660 km

(d)

[%] Vs

| 2.0 |
| 1.2 |
| 0.3 |
| -0.3 |
| -1.2 |
| -2.0 |

Topography Checkerboard

410

(e)

660

(f)

km

| 20 |
| 14 |
| 8 |
| 2 |
| -2 |
| -8 |
| -14 |
| -20 |

400−530 km

(g)

530−660 km

(h)

Figure 5. Resolution test for the joint inversion. The results for a checkerboard in the 530–660 km velocity anomaly layer are shown in the left column (maps a–d). The right-hand side column (maps e–h) shows the results for a checkerboard on the 660 km discontinuity. It is apparent that the trade-off between the two is negligible.

topography from their joint inversion and their previous *SS* precursor studies (Gu *et al.* 1998; Gu & Dziewonski 2002) and that their velocity did not change noticeably when accounting for discontinuity topography.

Both methods work equally well for reducing the effect of upper-mantle velocity heterogeneity on the precursor times and find the same average transition zone thickness, 240 km. However, the average 410 and 660 km discontinuity depths from the velocity-corrected model are different than those from the joint inversion model. Values for the average 410 km discontinuity depth range from 410 to 420 km while the average 660 is consistently found at 654 km (Flanagan & Shearer 1998a; Gu *et al.* 1998; Lawrence & Shearer 2006b). Absolute depths derived from *SS-SdS* times are very sensitive to the choice of the 1-D velocity model, and we caution against interpreting the absolute depths derived from *SS* precursors. For the joint inversion, we observe that there is almost no trade-off between the velocity and topography structure, therefore, it is acting essen-

tially as a computationally intensive velocity correction. Although shorter wavelength structure is present in the joint inversion model, the model does not fit the cap depths any better than the velocity-corrected model. In fact, the velocity-corrected model provides a slightly better fit to the cap depths. Therefore, we find that the direct correction for a known velocity model is the most straightforward and accurate method for reducing the effect of the upper-mantle and transition zone velocity anomalies and the corresponding model shown in Fig. 7 will be used for further analysis.

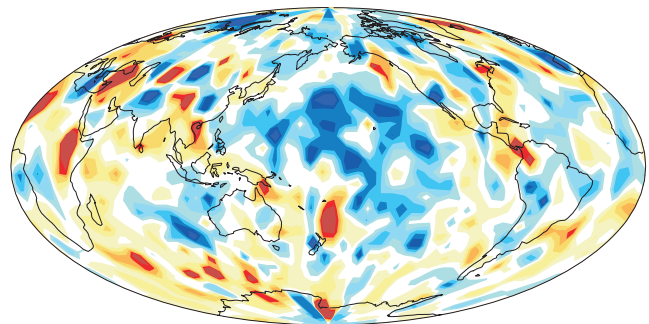## 5 COMPARISON TO PREVIOUS STUDIES

The deviations from the average transition zone width from this study (top), Gu *et al.* (2003) (middle left-hand side) and Flanagan & Shearer (1998a) (middle right-hand side) are shown Fig. 9. All

Joint Inversion Topography Results

Transition Zone Thickness

410 Topography

660 Topography

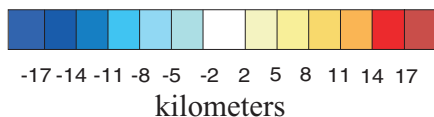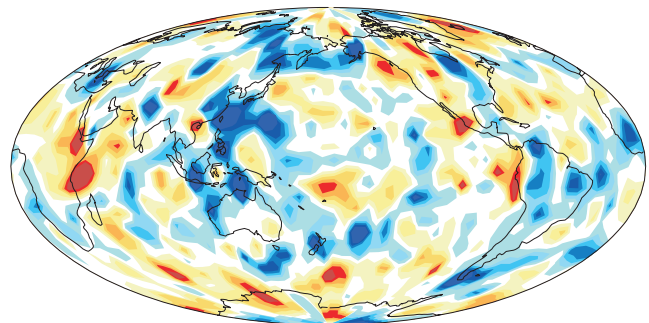-17 -14 -11 -8 -5 -2 2 5 8 11 14 17
kilometers
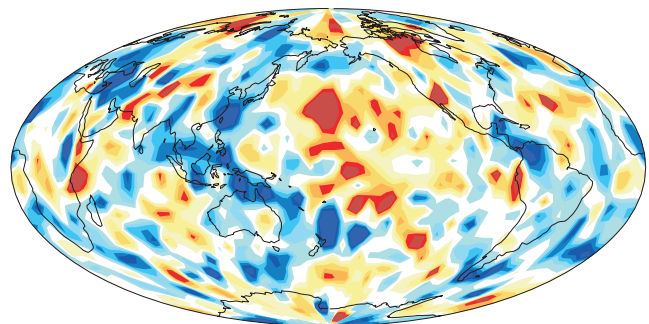
Figure 6. Deviations from the average 410 (middle panel) and 660 (bottom panel) km discontinuity depth and transition zone thickness (top) from the joint inversion for velocity anomalies and boundary topography. The average depths for the 410 and 660 km discontinuities from the joint inversion are 420 and 660 km, respectively, resulting in an average transition zone thickness of 240 km.

the maps are based on correcting their respective raw *SS–SdS* times for CRUST 2.0 and the 6° velocity model used to produce Fig. 7. Thus, any observed differences reflect differences in the data and not the corrections. Gu *et al.* (2003) performed a stacking procedure similar to that used here, but measure *SS–SdS* by cross-correlating the stacked trace with a synthetic seismogram. Their transition zone thickness is in good agreement with ours, which is shown quantitatively by the positive correlation (black line) at low harmonic

degrees in the bottom left of Fig. 9. Our transition zone thickness is highly correlated (bottom right-hand side, black line) with Flanagan & Shearer (1998a), as would be expected since their data is included in this study. Our map of transition zone thickness is more detailed and has higher amplitude than the Gu *et al.* (2003) and Flanagan & Shearer (1998a) maps because our increased data set allows us to reduce the stacking cap size from the 10° radius used in the previous studies to just 5° radius.

Our results are useful for examining local *SS* precursor results in a broader context. Our 410 km discontinuity topography map generally agrees with the globally distributed 2-D *S410S* stacks of Deuss & Woodhouse (2002). *SS* precursors have been used to investigate hotspot regions in the vicinity of the Society (Niu *et al.* 2002) and Hawaii (Schmerr & Garnero 2006) Islands where the transition zone is found to be thinner than average, in agreement with our result that the transition zone is thin beneath most of the Pacific. However, Lee & Grand (1996) use *SS* precursors to determine that the transition zone is average in thickness beneath the East Pacific Rise. Our result that the transition zone is generally thin in the Pacific complicates the interpretation that a thin transition zone indicates the presence of a lower-mantle heat source beneath Pacific hotspots.

Recently, mapping of the discontinuities has been attempted with *PP* precursors. We performed our stacking analysis to identify *PP* precursors, but found the results very unstable. The *P410P* and *P660P* most often are indistinguishable from the noise. The *PP* stacks are also available from the corresponding author's website. Deuss *et al.* (2006) suggest that a complex chemical structure is necessary to explain the variations they see in *P660P*. However, the variation may just be an artefact of the difficulty in detecting *P660P*. Chambers *et al.* (2005) use *P410P* and *S410S* to produce individual and joint maps of global 410 km discontinuity topography. Whereas the long wavelength features of their *S410S* 410 topography map are in agreement with our results, some features are quite different, most notably, in the western Pacific where their 410 topography shallows and ours deepens. This feature is also present in their *P410P* map, but not in the Flanagan & Shearer (1999) *P410P* map. Their 410 topography maps also have more power at spherical harmonic degree two, while the power in our 410 topography is concentrated at degree one in agreement with Flanagan & Shearer (1998a, 1999) and Gu *et al.* (2003). The cause of these discrepancies is unknown, but is likely related to differences in the waveform stacking procedures.

6 INTERPRETATION

So far, we have determined that our preferred transition zone thickness and 410 and 660 km discontinuity topography are derived from the crust and velocity-corrected *SS–SdS* times calculated by stacking the combined (F&S and cluster analysis) data set of *SS* peak times. By comparing the structure in the crust and velocity corrections with that in the topography models before and after the corrections (see online Supplementary Material), we believe that we have removed a majority of the structure above the transition zone from influencing the discontinuity topography. Therefore, our maps of discontinuity topography and transition zone thickness can be interpreted in terms of the thermochemical variations. Theoretical and experimental mineral physics have shown that the phase transformation of α-olivine to β-spinel (wadsleyite) occurs at approximately 410 km depth and that the γ-spinel (ringwoodite) to perovskite and magnesiowustite occurs at approximately 660 km depth (Anderson
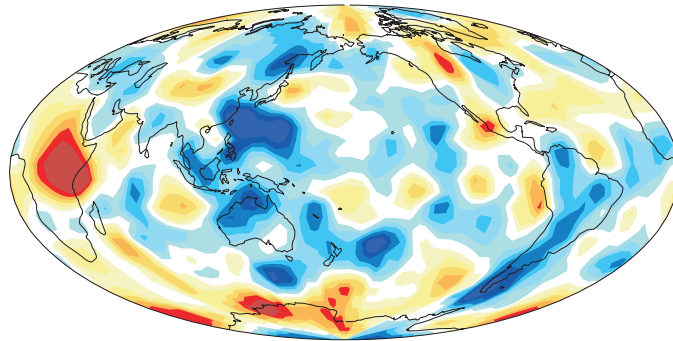
Crust and Velocity Corrected Discontinuities
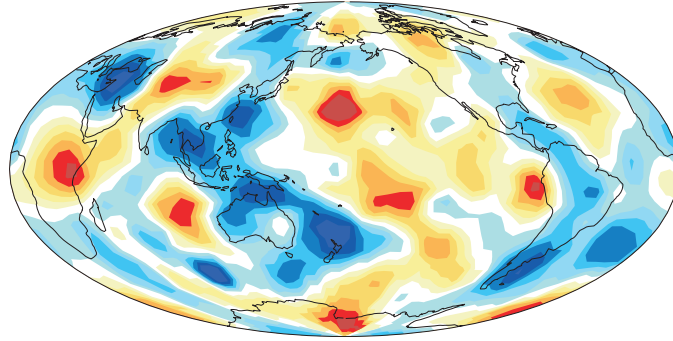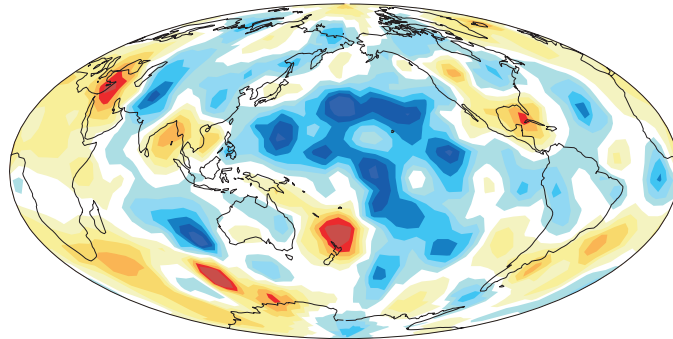
Transition Zone Thickness

410 Topography

660 Topography

Figure 7. Deviations from the average 410 (middle panel) and 660 (bottom panel) km discontinuity depth and transition zone thickness (top panel) corrected for CRUST 2.0 and the 6° shear velocity model described in section 4.1. The map is computed using spherical splines, which are equivalent to a spherical harmonic expansion out to degree 20. The average depths of the 410 and 660 km discontinuities are 410 and 650 km, respectively, resulting in an average transition zone thickness of 240 km using 20 s PREM.

1967; Ringwood 1969; Ita & Strixrude 1992; Helffrich 2000). It is thought that the β-spinel (wadsleyite) to γ-spinel (ringwoodite) transition occurs at around 520 km causing the less pronounced 520 km discontinuity (Shearer 1990, 1996; Deuss & Woodhouse 2001).

Although the phase transformations occur in a composite material with interactions among the chemical species MgO, FeO, SiO$_2$, CaO and Al$_2$O$_3$, we can approximate the behaviour of the transformation as a single component system. In a single component system, the Clapeyron slope, dP/dT, the change in pressure over the change in temperature, can be used to predict the behaviour of a phase change in response to a thermal anomaly. The Clapeyron slopes for the transformations occurring at the 410 and 660 km discontinuities are positive and negative, respectively. Therefore, in the presence

Correlation and Amplitude of the Velocity Corrected Versus the Joint Inversion Topography

410
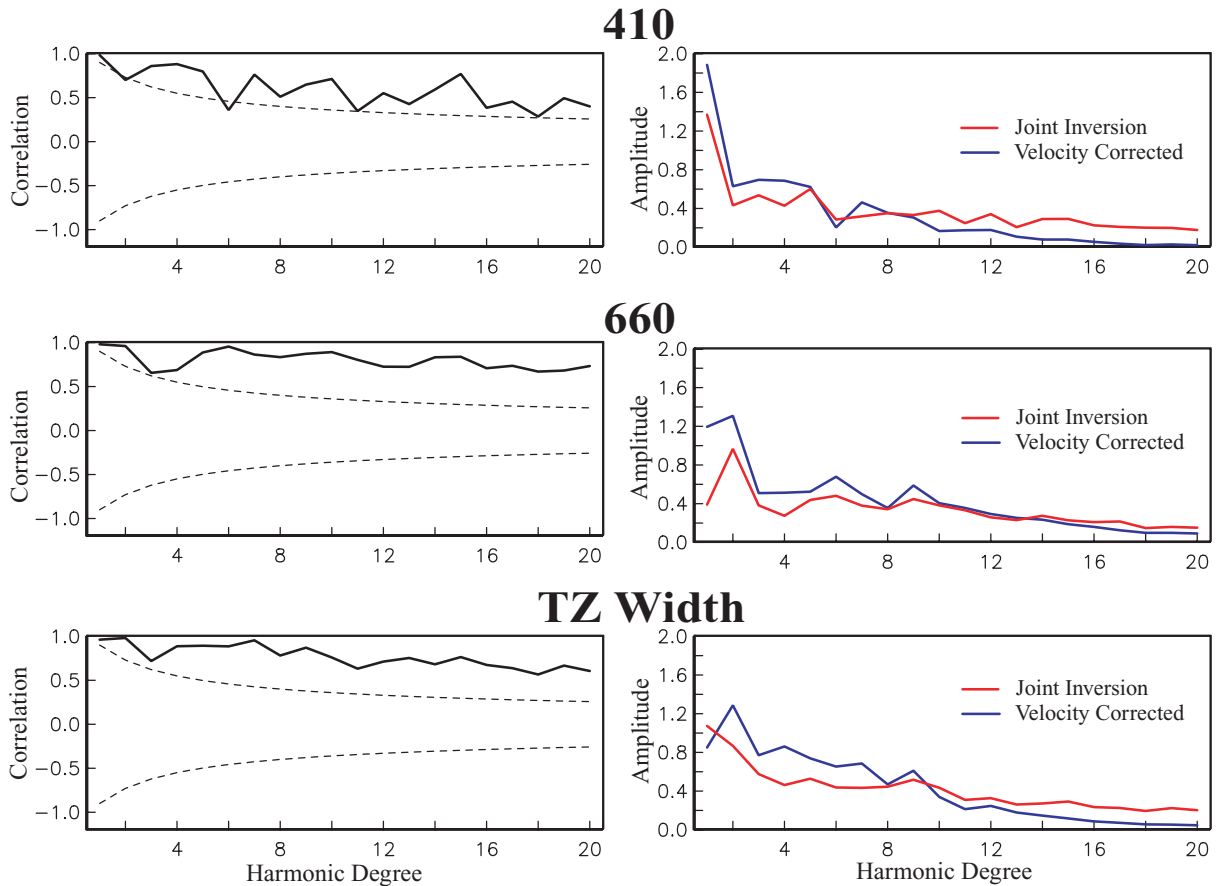

660

TZ Width

Figure 8. Left-hand panel: The correlation of the joint inversion discontinuity topography and transition zone thickness to that from the velocity-corrected model. Right-hand panel: The amplitude of the velocity-corrected (blue) and joint inversion (red) depths as a function of harmonic degree. The dashed lines represent the 90 per cent significance level for positive and negative correlations.

of a vertically coherent cold thermal anomaly, the transition zone should be thicker than average and thinner in the presence of a warm thermal anomaly.

If the 410 and 660 km discontinuities are undulating in response to thermal variations, we expect the transition zone thickness to be anticorrelated with the velocity anomalies in the transition zone. For example, a negative, or slow, velocity anomaly caused by a decrease in temperature should cause the transition zone to thin, which is a positive anomaly based on our sign conventions. This phenomena is shown to be true in Fig. 10, which shows the velocity and crust-corrected transition zone thickness alongside the 6° shear velocity anomaly model, as well as the correlation of the thickness to each velocity layer and the associated amplitudes as a function of harmonic degree. The transition zone thickness and velocity structure are highly anticorrelated, although there is an absence of correlation at degree one. This seems to support the idea that the long-wavelength features of the 410 and 660 km discontinuity topography could indeed be caused by their respective phase transformations moving to shallower or deeper depths in response to vertically coherent thermal anomalies.

On the other hand, if a vertically coherent thermal anomaly is affecting the 410 and 660 km discontinuities, then it is expected that their topography would be opposite to each other, or anticorrelated,

due to the opposite signs of the Clapeyron slopes associated with their phase changes. However, in Fig. 11 it is clear that, overall, the 410 and 660 km discontinuities are somewhat positively correlated or uncorrelated rather than anticorrelated, which appears to contrast with the correlation of the transition zone thickness with the velocity anomalies. Fig. 12 (top panel) shows the correlation and amplitude of the 410 km discontinuity topography with the shear velocity model in the layer between 400 and 530 km. Likewise, Fig. 12 (bottom panel) is the correlation and amplitude of the 660 km discontinuity topography with the shear velocity model in the layer between 530 and 660 km. The amplitude of the 660 km discontinuity topography is similar to that of the 410 km discontinuity except that it is noticeably higher at degree two (Fig. 11), which is also the dominant signal in the velocity structure.
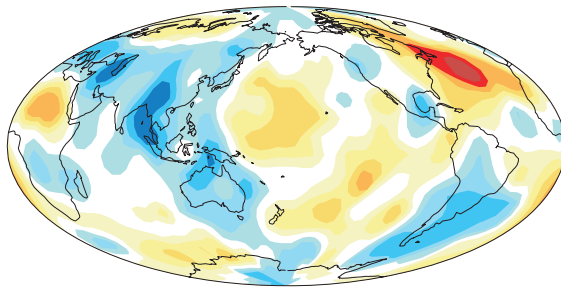
One explanation for the apparent discrepancy is that the thermal structure is not vertically coherent between the two discontinuities. This is doubtful since the velocity structure (a likely proxy for the thermal structure) at the 410 and 660 km discontinuities is similar, although there is some degree of vertical smearing of structure in the transition zone due to the broad depth sensitivities of our long-period surface waves. The correlation of the 410 and 660 km discontinuity topography has also been found by Gu *et al.* (1998). As discussed previously and summarized in Collier *et al.* (2001),
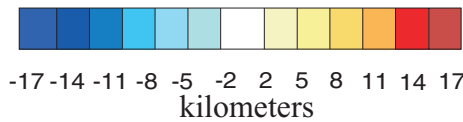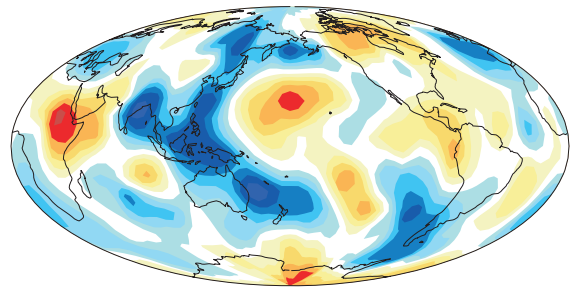
Transition Zone Thickness Comparison

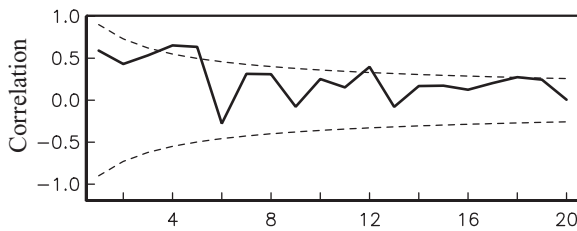## Our Combined Data: Velocity and Crust Corrected
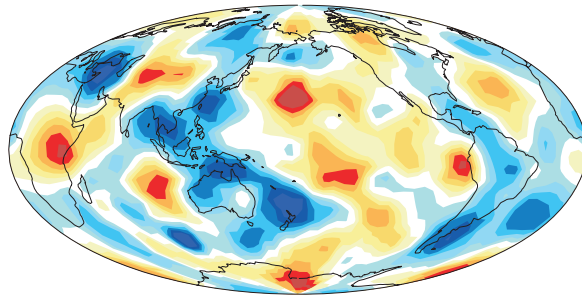
GDE 2003: Velocity and Crust Corrected   **F&S 1998a: Velocity and Crust Corrected**

-17 -14 -11 -8 -5 -2 2 5 8 11 14 17
kilometers

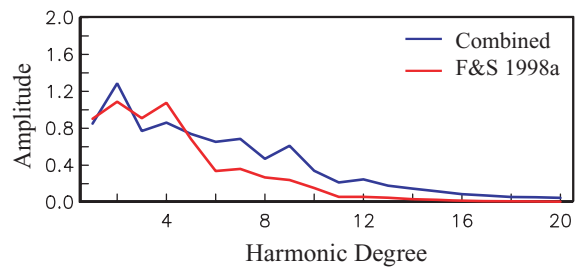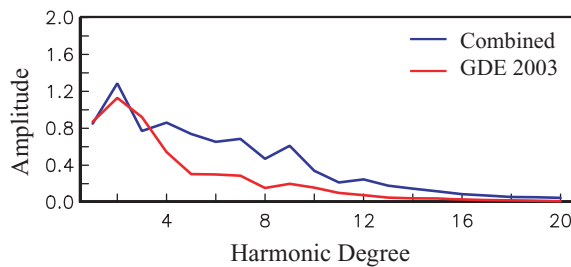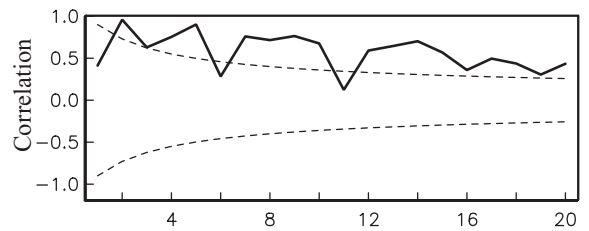**Our Combined Data vs. GDE 2003**   **Our Combined Data vs. F&S 1998a**

Figure 9. Comparison of our transition zone thickness (top panel) to that from Gu *et al.* (2003) (middle left-hand panel) and Flanagan & Shearer (1998a) (middle right-hand panel). The bottom graphs are the correlation and amplitude as a function of harmonic degree for our map of transition zone thickness versus that of Gu *et al.* (2003) (left-hand panel) and Flanagan & Shearer (1998a) (right-hand panel). The dashed lines are the 90 per cent confidence levels for positive and negative correlations.

studies of reflected and converted phases in subduction zones do find the discontinuities to be anticorrelated on scales of hundreds of kilometres. In the western Pacific between the Java and Tonga trenches, we also see a deep 660 km discontinuity accompanied by a shallow 410 km discontinuity. Therefore, it is likely that the 410 km discontinuity does respond as expected in the presence of a thermal anomaly. The fact that it is not globally anticorrelated with the 660 km discontinuity or correlated with the velocity structure indicates that other
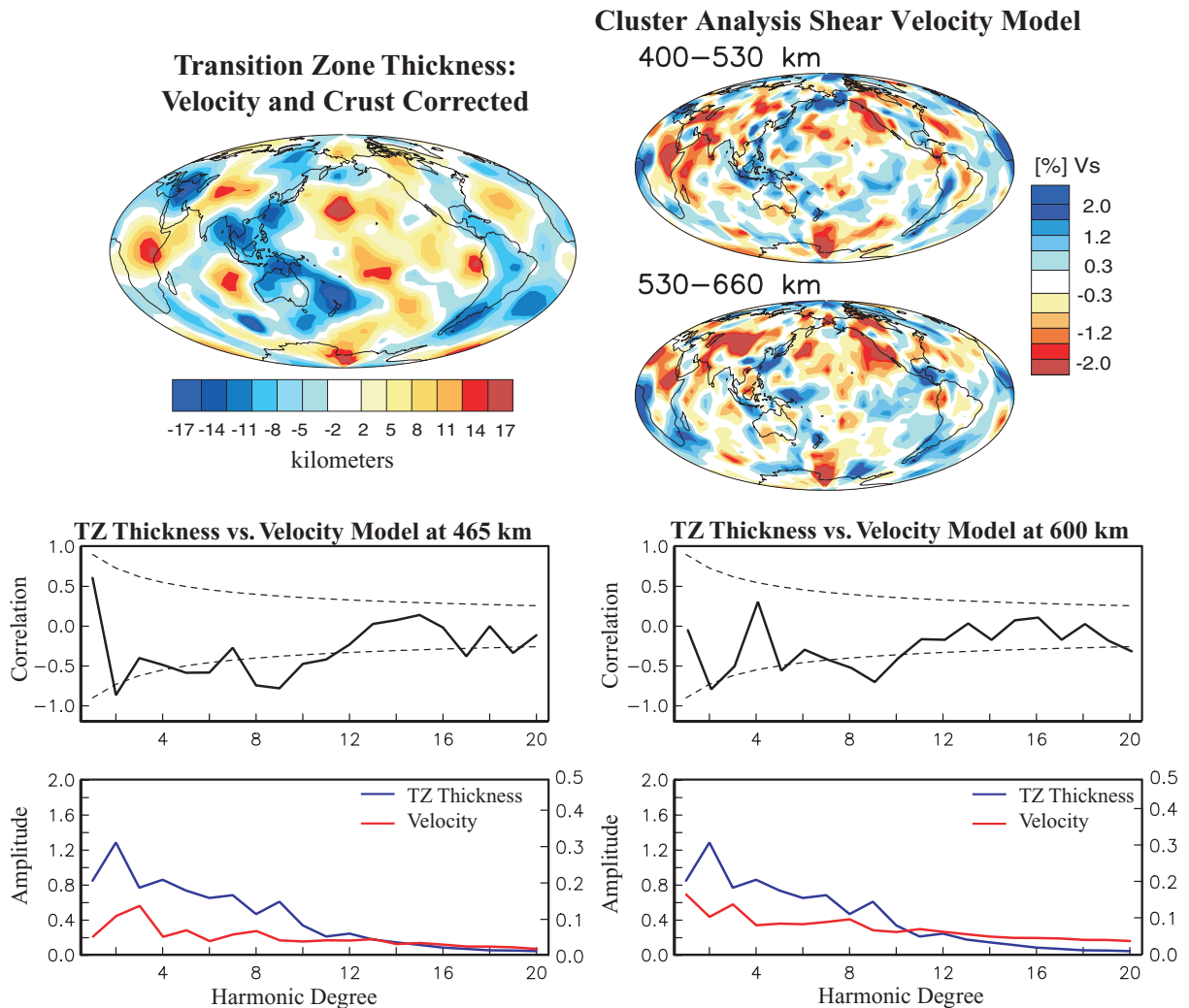
**Transition Zone Thickness:
Velocity and Crust Corrected**

Cluster Analysis Shear Velocity Model
400−530 km

Figure 10. Top left-hand panel: Our crust and velocity corrected transition zone thickness. Top right-hand panel: Our 6° shear velocity model based on Houser *et al.* (2008) for layers in the transition zone. Bottom left-hand panel: The correlation and amplitude of the transition zone thickness with the velocity model layer between 400 and 530 km. Bottom right-hand panel: The correlation and amplitude of the transition zone thickness with the velocity model layer between 530 and 660 km. The dashed lines in the correlation plot represent the 90 per cent significance level for positive and negative correlations. The scale on the right hand side of the amplitude is that for velocity (red) and the left side for thickness (blue) as a function of harmonic degree. The high anticorrelation between the thickness and the velocities (except at degree 1) implies that the transition zone thickness is responding to the same thermal structure that causes the velocity anomalies.

factors must be contributing to the 410 km discontinuity topography. However, the long wavelength features of the 660 km discontinuity topography and transition zone thickness are correlated to the velocity structure. This can be explained by the depression of the ringwoodite to perovskite and magnesiowustite phase change due to the ponding of cold subducted oceanic lithosphere. This ponding was first discovered by Shearer & Masters (1992) from the mapping *S660S*, but was brought into question by Petersen *et al.* (1993). However, the depression of the 660 km discontinuity in the western Pacific is a robust feature (Shearer 2000). The ponding is likely due, in part, to the effect of the endothermic phase change of ringwoodite to perovskite and magnesiowustite phase change which inhibits the flow of cold material into the lower mantle. A high-viscosity lower mantle (Forte & Mitrovica 2001) could also impede flow across the 660 km discontinuity. Further modelling is necessary to understand the balance of these forces, which could contribute to the temporary resistance to flow from the upper to lower mantle.

Since the 410 km discontinuity exhibits behaviour that is not expected from simple Clapeyron slope arguments, there is likely a contribution from compositional variations. Weidner & Wang (2000) have demonstrated that a variety of behaviours for 410 km discontinuity topography can be expected depending on the concentration of aluminium and iron. Other studies (Vinnik & Farra V. 2002; Bercovici & Karato 2003; Song *et al.* 2004) have suggested that melt may be present at the 410 km discontinuity. Bercovici & Karato (2003) propose that the melt occurs when material upwelling across the wadsleyite–olivine boundary looses its water due to wadsleyite having the ability to incorporate more water into its silicate structure than olivine. This proposed, and sometimes observed (Song *et al.* 2004), melt layer, although thin, would have a greater impact on the amplitude of *S410S* than on the timing of the phase arrival. However, their model requires that the melt layer be ubiquitous and, therefore, would effect the observed mean *S410S* time rather than its lateral variations. Recently, Jacobsen & Smyth (2006) describe
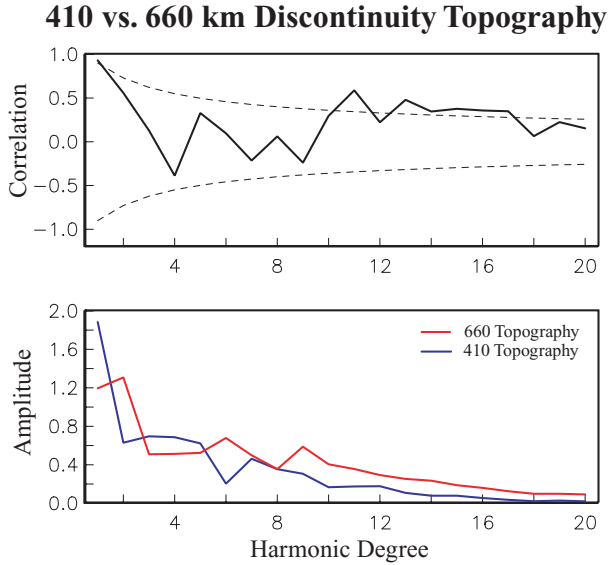
410 vs. 660 km Discontinuity Topography

Figure 11. Correlation (top panel) and amplitude (bottom panel) of the 410 (blue) and 660 (red) km discontinuity topography versus harmonic degree. From the expected Clapeyron slopes, the 410 and 660 km discontinuities should be anticorrelated for a vertically coherent thermal anomaly. The dashed lines represent the 90 per cent significance level for positive and negative correlations.

a scenario in which the 410 and 660 km discontinuities are anticorrelated and accompanied by high *Vp/Vs* ratios due to the presence of a few percent water. This scenario does not agree with our findings since it also indicates that the 410 and 660 km discontinuities should be anticorrelated and that a shallow 410 km discontinuity should correspond to regions of slow shear velocities, which we do not observe. To date, the chemical and mineralogical implications of the curious topography of the 410 km discontinuity has to be fully explored.

It is also necessary to address the issue of the amplitudes of the 410 and 660 km discontinuities. It has long been observed that topography on the 410 km discontinuity is smaller than that on the 660 km discontinuity (Helffrich 2000; Shearer 2000). This observation runs counter to the observation that the Clapeyron slopes of the phase changes occurring at the 410 and 660 km discontinuities, while opposite in sign, have a similar magnitude (Bina & Helffrich 1994). However, since we have demonstrated that the 410 km discontinuity topography likely has a significant compositional component, differences in the discontinuity topography magnitude may not reflect differences in their respective Clapeyron slopes. In Fig. 11, the amplitudes of the 410 km (blue) and the 660 km (red) discontinuity topography are similar. This indicates that the 410 km discontinuity may have as much topography as the 660 km discontinuity.

Fig. 13 shows histograms of the 410 and 660 km discontinuity topography in each 5° radius bin from the F&S study (top panel), our combined data set (middle panel) and our combined data set with more than 40 traces contributing to the stacked trace (bottom panel). If the 410 km discontinuity truly has less topography than the 660 km discontinuity, the histogram of 410 km discontinuity topography should be narrower than that of 660 km discontinuity topography. However, it is apparent from the histograms that the 410 and 660 km discontinuity depth variations have similar magnitude. It is interesting to note that the width of the histograms has not changed from the F&S study to our combined data. The width of
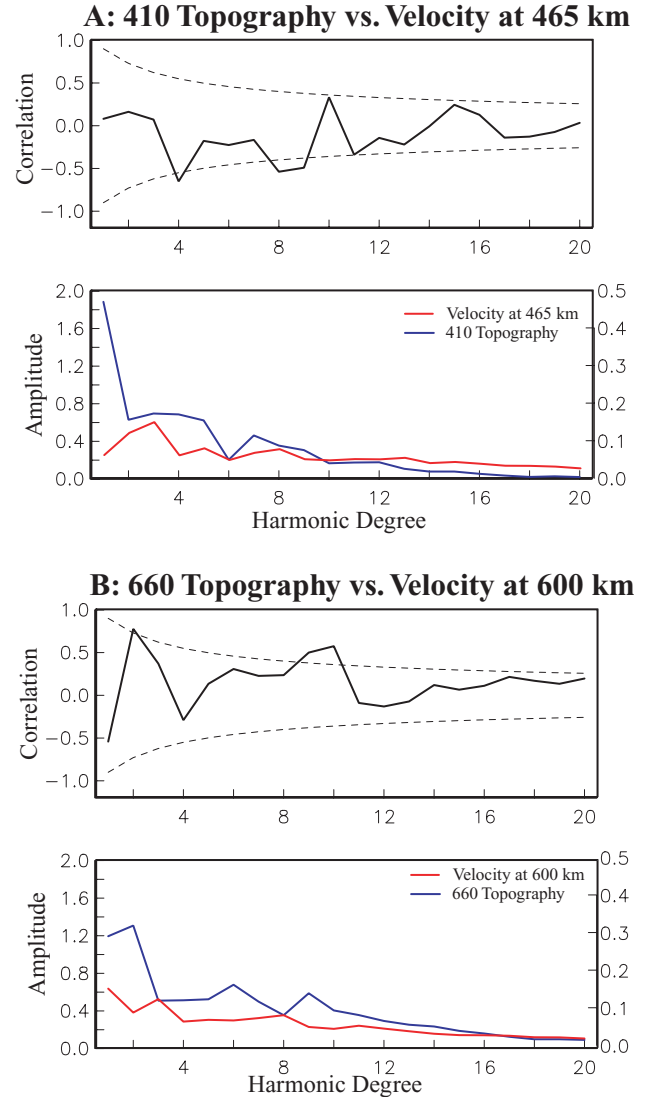
A: 410 Topography vs. Velocity at 465 km

B: 660 Topography vs. Velocity at 600 km

Figure 12. (A) The correlation (top panel) and amplitude (bottom panel) of our 410 km discontinuity topography (blue) and velocity structure in the layer between 400 and 530 km (red) versus harmonic degree. (B) The correlation (top panel) and amplitude (bottom panel) of our 660 km discontinuity topography (blue) and velocity structure in the layer between 530 and 660 km (red) versus harmonic degree. The velocities are from a 6° cluster analysis shear velocity model derived from Houser *et al.* (2008). The dashed lines represent the 90 per cent significance level for positive and negative correlations. The scales on the right- and left-hand side of the amplitude plot are for velocity (red) and topography (blue), respectively.

the histogram for the 410 km discontinuity topography is somewhat narrower than that of the 660 km discontinuity topography for the stacks of the combined data set with more than 40 traces; although this requirement limits the analysis mostly to the northwestern Pacific and may not representative of global structure. Therefore, we conclude that the topography on the 410 km discontinuity is not significantly less than, but is comparable to, the topography on the 660 km discontinuity.

7 CONCLUSIONS

(1) We have used the cluster analysis *SS* arrival times to find the maximum of the *SS* pulse to join our data set with the data set of

410 Topography   660 Topography

Flanagan and Shearer 1998a

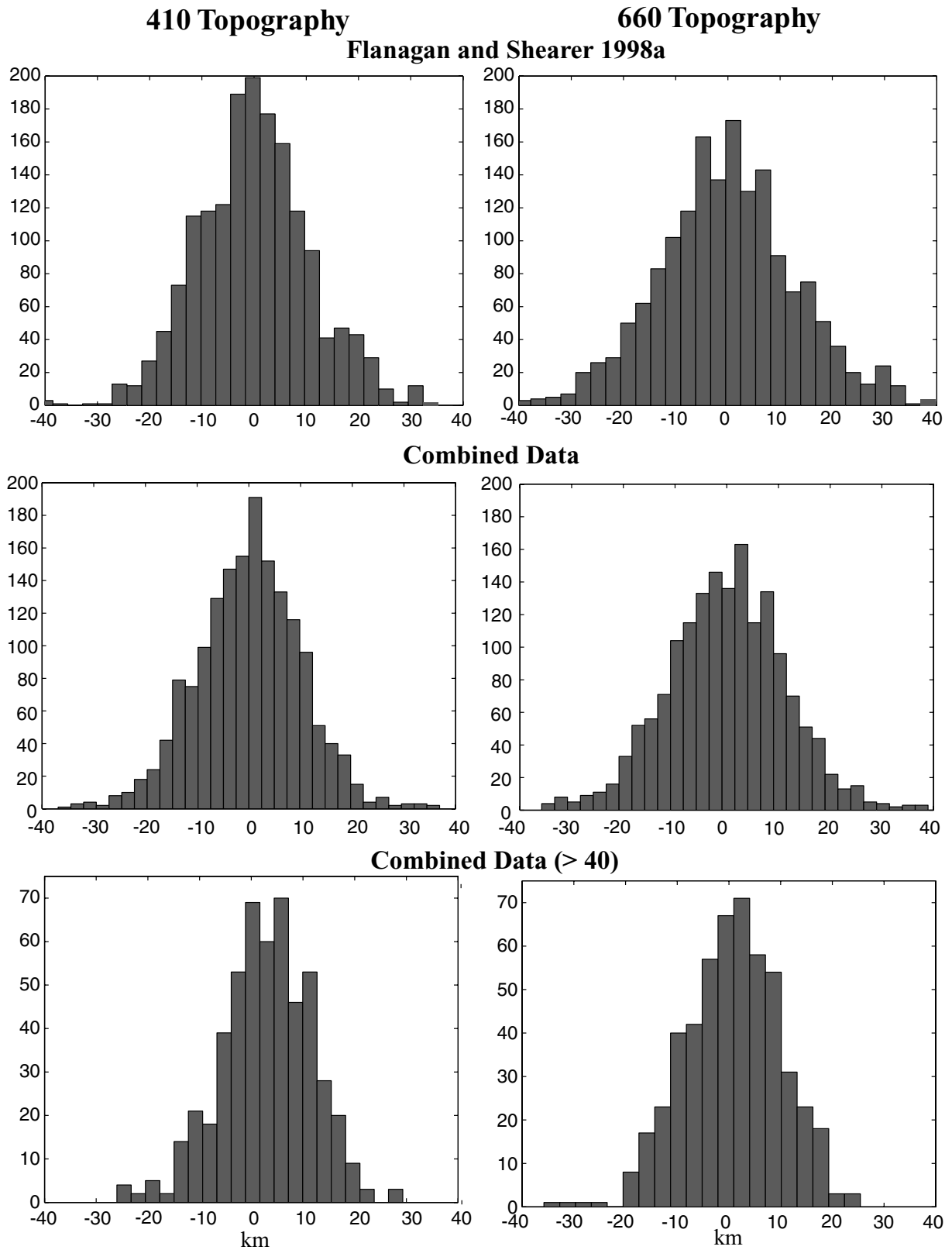### Combined Data

Combined Data (> 40)

Figure 13. Histograms of the F&S (top row), our combined (middle row) and our combined with greater than 50 traces in a stack (bottom row) 410 and 660 discontinuity depths. *Note:* The scale on the bottom histograms is about a third that of the top and middle histograms. The 410 km discontinuity topography histogram narrows somewhat for caps with greater than 40 traces, but the restriction limits the bins to geographically well-sampled regions such as the northwestern Pacific (see Fig. 2).

Flanagan & Shearer (1998a). By combining the data sets, we have more than tripled the number of traces used in the original F&S study. Our cluster analysis method allows each of the traces to be visually inspected, but traveltimes from vast amounts of data can be determined quickly compared with the completely manual analysis used in the F&S study. The resulting 410 and 660 km discontinuity topography and transition zone thickness are very similar to those in the F&S study, demonstrating that our *SS* maximum times are compatible with those determined manually. Therefore, it is not necessary to manually determine the maximum of the *SS* pulse for stacking.

(2) We have explored two means of correcting for the effect of the velocity structure on the precursor times. The first approach is to jointly invert for velocity and boundary perturbations. However, the results from this method are essentially the same as removing the calculated traveltime anomaly from a known velocity model. Since the latter method is computationally inexpensive and fits the data equally well or better, we prefer to apply a crust and velocity correction to reduce their influence on our estimates of the 410 and 660 km discontinuity topography and transition zone thickness.

(3) Our results agree with most *SS* precursor studies including those of Gu & Dziewonski (2002) and Gu *et al.* (2003) which use similar data and methods.

(4) We have shown that the transition zone width and 660 km discontinuity topography are correlated to transition zone velocity structure, but the 410 km discontinuity is uncorrelated. In addition, the 410 km discontinuity topography is slightly correlated rather than anticorrelated with the 660 km discontinuity as would be expected for a vertically coherent thermal anomaly. This implies that there are probable compositional variations affecting the olivine to wadsleyite phase transition in the region of the 410 km discontinuity.

(5) We have found similar amplitudes of the 410 and 660 km discontinuity topography for our combined data which contradicts previous studies that have found less topography on the 410 km discontinuity.

ACKNOWLEDGMENTS

REFERENCES

Ai, Y., Zheng, T., Xu, W., He, Y. & Dong, D., 2005. A complex 660 km discontinuity beneath northwestern China, *Earth planet. Sci. Lett.,* **212,** 63–71.

Amnon, C., 1991. Isolation of receiver effects from teleseismic P waveforms, *Bull. seism. Soc. Am.,* **82,** 2504–2510.

Anderson, D., 1967. Phase changes in the upper mantle, *Science,* **157,** 1165–1173.

Bassin, G., Laske, G. & Masters, G., 2000. The current limits of resolution for surface wave tomography in North America, *Trans. Am. Geophys. Union,* **81,** 897.

Bercovici, D. & Karato, S.-I., 2003. Whole-mantle convection and the transition-zone water filter, *Nature,* **425,** 39–44.

Bina, C. & Helffrich, G., 1994. Phase transition Clapeyron slopes and transition zone seismic discontinuity topography, *J. geophys. Res.,* **99,** 15 853–15 860.

Blum, J. & Shen, Y., 2004. Thermal, hydrous, and mechanical states of the mantle transition zone beneath southern Africa, *Earth planet. Sci. Lett.,* **217,** 367–378.

Bostock, M., 1996. *Ps* conversions from the upper mantle transition zone beneath the Canadian landmass, *J. geophys. Res.,* **101,** 8393–8402.

Castle, J. & Creager, K., 1998. Topography of the 660-km seismic discontinuity beneath Izu-Bonin: implications for tectonic history and slab deformation, *J. geophys. Res.,* **103,** 12 511–12 527.

Chaljub, E. & Tarantolla, A., 1997. Sensitivity of *SS* precursors to topography on the upper-mantle 660-km discontinuity, *Geophys. Res. Lett.,* **24,** 2613–2616.

Chambers, K., Woodhouse, J.H. & Deuss, A., 2005. Topography of the 410 km discontinuity from *PP* and *SS* precursors, *Earth planet. Sci. Lett.,* **235,** 610–622.

Chen, Y., Roecker, S. & Kosarev, G., 1997. Elevation of the 410 km discontinuity beneath the central Tien Shan: evidence for a detached lithospheric root, *Geophys. Res. Lett.,* **24,** 1531–1534.

Chevrot, S., Vinnik, L., & Montagner, J.-P., 1999. Global-scale analysis of the mantle *Pds* phases, *J. geophys. Res.,* **104,** 20 203–20 219.

Collier, J. & Helffrich, G., 1997. Topography of the '410' and '660' km seismic discontinuities in the Izu-Bonin subduction zone, *Geophys. Res. Lett.,* **24,** 1535–1538.

Collier, J., Helffrich, G. & Wood, B., 2001. Seismic discontinuities in subduction zones, *Phys. Earth planet. Inter.,* **127,** 35–49.

Deuss, A. & Woodhouse, J.H., 2001. Seismic observations of splitting of the mid transition zone discontinuity, *Science,* **294,** 345–357.

Deuss, A. & Woodhouse, J.H., 2002. A systematic search for mantle discontinuities using *SS*-precursors, *Geophys. Res. Lett.,* **29,** doi:10.1029/2002GL014768.

Deuss, A., Redfern, S., Chambers, K. & Woodhouse, J.H., 2006. The nature of the 660-kilometer discontinutiy in Earth's mantle from global observations of *PP* precursors, *Science,* **311,** 198–201.

Dueker, K. & Sheehan, A., 1997. Mantle discontinuity structure from midpoint stacks of converted *P* to *S* waves across the Yellowstone hotspot track, *J. geophys. Res.,* **102,** 8313–8327.

Dueker, K. & Sheehan, A., 1998. Mantle discontinuity structure beneath the Colorado Rocky Mountains and High Plains, *J. geophys. Res.,* **103,** 7153–7169.

Dziewonski, A. & Anderson, D., 1981. Preliminary reference Earth model, *Phys. Earth planet. Inter.,* **25,** 297–356.

Dziewonski, A.M. & Gilbert, F., 1976. The effect of small, aspherical perturbations on travel times and a re-examination of the corrections for ellipticity, *Geophys. J. R. astr. Soc.,* **44,** 7–18.

Flanagan, M. & Shearer, P., 1998a. Global mapping of topography on transition zone discontinuities by stacking of *SS* precursors, *J. geophys. Res.,* **103,** 2673–2692.

Flanagan, M. & Shearer, P., 1998b. Topography on the 410-km seismic velocity discontinuity near subduction zones from stacking of *sS*, *sP*, and *pP* precursors, *J. geophys. Res.,* **103,** 21 165–21 182.

Flanagan, M. & Shearer, P., 1999. A map of topography on the 410-km discontinuity from *PP* precursors, *Geophys. Res. Lett.,* **26,** 549–552.

Forte, A. & Mitrovica, J., 2001. Deep-mantle high-viscosity flow and thermochemical structure inferred from seismic and geodynamic data, *Nature,* **410,** 1049–1056.

Gao, S., Silver, P., Liu, K. & the Kaapvaal Seismic Group, 2002. Mantle discontinuities beneath Southern Africa, *Geophys. Res. Lett.,* **29,** doi:10.1029/2001GL013834.

Gilbert, H., Sheehan, A., Dueker, K. & Molnar, P., 2003. Receiver function in the western United States, with implications for upper mantle structure and dynamics, *J. geophys. Res.,* **108,** doi:10.1029/2001JB001194.

Gu, Y. & Dziewonski, A., 2002. Global variability of transition zone thickness, *J. geophys. Res.,* **107,** doi:10.1029/2001JB000489.

Gu, Y., Dziewonski, A. & Agee, C., 1998. Global de-correlation of the topography of transition zone discontinuities, *Earth planet. Sci. Lett.,* **157,** 57–67.

Gu, Y., Dziewonski, A. & Ekstrom, G., 2003. Simultaneous inversion for mantle shear velocity and topography of transition zone discontinuities, *Geophys. J. Int.,* **154,** 559–583.

Gurrola, H. & Minster, B., 1998. Thickness estimates of the upper-mantle transition zone from bootstrapped velocity spectrum stacks of receiver functions, *Geophys. J. Int.,* **133,** 31–43.

Helffrich, G., 2000. Topography of the transition zone seismic discontinuities, *Rev. Geophys.,* **38,** 141–158.

Hooft, E., Toomey, D. & Solomon, S., 2003. Anomalously thin transition zone beneath the Galapagos hotspot, *Earth planet. Sci. Lett.,* **216,** 55–64.

Houser, C., Masters, G., Shearer, P. & Laske, G., 2008. Shear and compressional velocity models of the mantle from cluster analysis of long-period waveforms, *Geophys. J. Int.,* doi:10.1111/j.1365-246X.2008.03763.x.

Ita, J. & Strixrude, L., 1992. Petrology, elasticity, and composition of the mantle transition zone, *J. geophys. Res.,* **97,** 6849–6866.

Jacobsen, S.D. & Smyth, J.R., 2006. Effect of water on the sound velocities of ringwoodite in the transition zone in *Earth's Deep Water Cycle,* Vol. 168, pp. 131–145, eds, Jacobsen, S. & van der Lee, S., American Geophysical Union, Washington, D.C.

Kind, R. & Vinnik, L., 1988. The upper-mantle discontinuities underneath the GRF array from *P*-to-*S* converted phases, *J. geophys. Res.,* **62,** 138–147.

Langston, C., 1979. Structure under Mount Rainier, Washington, inferred from teleseismic body waves, *J. geophys. Res.,* **84,** 4749–4762.

Lawrence, J. & Shearer, P., 2006a. A global study of transition zone thickness using receiver functions, *J. geophys. Res.,* **111,** doi:10.1029/2005JB003973.

Lawrence, J. & Shearer, P., 2006b. Constraining seismic velocity and density for the mantle transition zone with reflected and transmitted waveforms, *Geochem. Geophys. and Geosyst.,* **7,** doi:10.1029/2006GC001339.

Lebedev, S., Chevrot, S. & van der Hilst, R., 2002. The 660-km discontinuity within the subducting NW-Pacific lithospheric slab, *Earth planet. Sci. Lett.,* **205,** 25–35.

Lebedev, S., Chevrot, S. & van der Hilst, R., 2003. Correlation between the shear-speed structure and thickness of the mantle transition zone, *Phys. Earth planet. Inter.,* **136,** 25–40.

Lee, D-K. & Grand, S., 1996. Depth of the upper mantle discontinuities beneath the East Pacific Rise, *Geophys. Res. Lett.,* **23,** 3369–3372.

Li, X., Kind, R., Priestly, K., Sobolev, S.V., Tilmann, F., Yuan, X. & Weber, M., 2000a. Mapping the Hawaiian plume conduit with converted seismic waves, *Nature,* **405,** 938–941.

Li, X., Sobolev, S.V., Kind, R., Yuan, X. & Estabrook, Ch., 2000b. A detailed receiver function image of the upper mantle discontinuities in the Japan subduction zone, *Earth planet. Sci. Lett.,* **183,** 527–541.

Li, X., Kind, R., Yuan, X., Sobolev, S.V., Hanks, W., Ramesh, D.S., Gu, Y. & Dziewonski, A., 2003. Seismic observation of narrow plumes in the oceanic upper mantle, *Geophys. Res. Lett.,* **30,** doi:1029/2002GL015411.

Masters, G., Johnson, S., Laske, G. & Bolton, H., 1996. A shear-velocity model of the mantle, *Phil. Trans. R. Soc. Lond. A.,* **354,** 1385–1411.

Neele, F., de Regt, H. & VanDecar, J., 1997. Gross errors in upper-mantle discontinuity topography from underside reflection data, *Geophys. J. Int.,* **129,** 194–204.

Niu, F. & Kawakatsu, H., 1995. Direct evidence for the undulation of the 660-km discontinuity beneath Tonga: comparison of Japan and California array data, *Geophys. Res. Lett.,* **22,** 531–534.

Niu, F., Solomon, S.C., Silver, P., Suetsugu, D. & Inoue, H., 2002. Mantle transition-zone structure beneath the South Pacific Superswell and evidence for a mantle plume underlying the Society hotspot, *Earth planet. Sci. Lett.,* **198,** 371–380.

Niu, F., Levander, A., Cooper, C., Lee, C.-T., Lenardic, A. & James, D., 2004. Seismic constraints on the depth and composition of the mantle keel beneath the Kaapvaal craton, *Earth planet. Sci. Lett.,* **224,** 337–346.

Owens, T., Nyblade, A., Gurrola, H. & Langston, C., 2000. Mantle transition zone structure beneath Tanzania, East Africa, *Geophys. Res. Lett.,* **27,** 827–830.

Paige, C. & Saunders, M., 1973. Solution of sparse indefinite systems of equations and leastsquares problems, Res. Rep. STAN-CS-73–399, Stanford University, Stanford, CA.

Parker, R.L., 1994. *Geophysical Inverse Theory,* p. 195, Princeton University Press, Princeton, N.J., USA.

Paulssen, H., 1985. Upper mantle converted waves beneath the NARS array, *Geophys. Res. Lett.,* **12,** 709–712.

Paulssen, H., 1988. Evidence for a sharp 670-km discontinuity as inferred from *P*-to-*S* converted waves, *J. geophys. Res.,* **93,** 10 489–10 500.

Petersen, N., Gossler, J., Kind, R., Stammler, K. & Vinnik, L., 1993. Precursors to *SS* and the structure of transition zone of the north-western Pacific, *Geophys. Res. Lett.,* **20,** 281–284.

Ramesh, D.S., Kind, R. & Yuan, X., 2002. Receiver function analysis of the North American crust and upper mantle, *Geophys. J. Int.,* **150,** 91–108.

Ramesh, D.S., Kawakatsu, H., Watada, S. & Yuan, X., 2005. Receiver function images of the central Chugoku region in the Japanese islands using Hi-net data, *Earth Planets Space,* **57,** 271–280.

Revenaugh, J. & Jordan, T.H., 1991. Mantle layering from ScS reverberations; 2, The transition zone, *J. geophys. Res.,* **96**(B12), 19 763–19 780.

Richards, M. & Wicks, C., 1990. *S-P* conversion from the transition zone beneath Tonga and the nature of the 670 km discontinuity, *Geophys. J. Int.,* **101,** 1–35.

Ringwood, A.E., 1969. Phase transformations in the mantle, *Earth planet. Sci. Lett.,* **5,** 401–412.

Ritsema, J., Hagerty, M. & Lay, T., 1995. Comparison of broad-band and short-period seismic wave-form stacks—implications for upper-mantle discontinuity structure, *Geophys. Res. Lett.,* **22,** 3151–3154.

Romanowicz, B., 2003. Global mantle tomography: progress status in the past 10 years, *Ann. Rev. Earth Planet. Sci.,* **31,** 303–328.

Saita, T., Suetsugu, D., Ohtaki, T., Takenaka, H., Kanjo, K. & Purwana, I., 2002. Transition zone thickness beneath Indonesia as inferred using the receiver function method for data from JISNET regional broadband seismic network, *Geophys. Res. Lett.,* **29,** doi:10.1029/2001GL013629.

Schmerr, N. & Garnero, E., 2006. Investigation of upper mantle discontinuity structure beneath the central Pacific using *SS* precursors, *J. geophys. Res.,* **111,** doi:10.1029/2005JB004197.

Shearer, P., 1990. Seismic imaging of upper-mantle structure with new evidence for a 520-km discontinuity, *Nature,* **344,** 121–126.

Shearer, P., 1991. Constraints on upper mantle discontinuities from observations of long-period reflected and converted phases, *J. geophys. Res.,* **96,** 18 187–18 182.

Shearer, P., 1993. Global mapping of upper mantle reflectors from long-period *SS* precursors, *Geophys. J. Int.,* **115,** 878–904.

Shearer, P., 1996. Transition zone velocity gradients and the 520-km discontinuity, *J. geophys. Res.,* **101,** 3053–3066.

Shearer, P., 2000. Upper mantle seismic discontinuities, in *Earth's Deep Interior: Mineral Physics and Tomography From the Atomic to the Global Scale,* pp. 115–131, eds, Karato, S.-I., Forte, A., Liebermann, R., Masters, G. & Stixrude, L., American Geophyical Union, Washington, D.C.

Shearer, P. & Flanagan, M., 1999. Seismic velocity and density jumps across the 410- and 660-kilometer discontinuities, *Science,* **285,** 1545–1548.

Shearer, P. & Masters, G., 1992. Global mapping of topography on the 660-km discontinuity, *Nature,* **355,** 791–796.

Shearer, P., Flanagan, M. & Hedlin, M., 1999. Experiments in migration processing of *SS* precursor observations to image upper-mantle discontinuity structure, *J. geophys. Res.,* **104,** 7229–7242.

Shen, Y., Solomon, S., Bjarnason, I. & Wolfe, C., 1998. Seismic evidence for a lower-mantle origin of the Iceland plume, *Nature,* **395,** 62–65.

Song, T.R., Helmberger, D. & Grand, S., 2004. Low velocity zone atop the 410 seismic discontinuity in the northwestern US, *Nature,* **427,** 530–533.

Stammler, K, Kind, R., Kosarev, G., Plesinger, A., Horalek, J., Quiyuan, L. & Vinnik, L., 1991. Broadband observations of *PS* conversions from the upper mantle in Eurasia, *Geophys. J. Int.,* **105,** 801–804.

Stankiewicz, J., Chevrot, S., van der Hilst, R. & de Wit, M., 2002. Crustal thickness, discontinuity depth, and upper mantle structure beneath

southern Africa: constraints from body wave conversions, *Phys. Earth planet. Inter.,* **130,** 235–251.

Tibi, R. & Wiens, D.A., 2005. Detailed structure and sharpness of upper mantle discontinuities in the Tonga subduction zone from regional broadband arrays, *J. geophys. Res.,* **110,** doi:10.1029/2004JB003433.

Tonegawa, T., Hirahara, K. & Shibutani, T., 2005. Detailed structure of the upper mantle discontinuities around the Japan subduction zone imaged by receiver function analyses, *Earth Planets Space,* **57,** 5–14.

van der Meijde, M., van der Lee, S. & Giardini, D., 2005. Seismic discontinuities in the Mediterranean mantle, *Phys. Earth planet. Inter.,* **148,** 233–250.

Vidale, J. & Benz, H.M., 1992. Upper-mantle seismic discontinuities and the thermal structure of subduction zones, *Nature,* **356,** 678–683.

Vinnik, L., 1977. Detection of waves converted from *P* to *SV* in the mantle, *Phys. Earth planet. Inter.,* **15,** 39–45.

Vinnik, L. & Farra V., 2002. Subcratonic low-velocity layer and flood basalts, *Geophys. Res. Lett.,* **29,** doi:10.1029/2001GL014064.

Vinnik, L., Avetisjan, R. & Mikhailova, N., 1983. Heterogeneities in the mantle transition zone from observations of *P*-to-*S* converted waves, *Phys. Earth planet. Inter.,* **33,** 149–163.

Vinnik, L., Kosarev, G. & Petersen, N., 1996. Mantle transition zone beneath Eurasia, *Geophys. Res. Lett.,* **23,** 1485–1488.

Weidner, D. & Wang, Y., 2000. Phase transformations; implications for mantle structure, in *Earth's Deep Interior: Mineral Physics and Tomography From the Atomic to Global Scale,* Vol. 117, pp. 215–235, eds, Karato, S.-I., Forte, A., Liebermann, R., Masters, G. & Stixrude, L., American Geophyical Union, Washington, D.C.

Wicks, C. & Richards, M., 1993. A detailed map of the 660-kilometer discontinuity beneath the Izu-Bonin subduction zone, *Science,* **261,** 1424–1427.

Woodward, R. & Masters, G., 1991a. Global upper mantle structure from long-period differential travel times, *J. geophys. Res.,* **96,** 6351–6377.

Woodward, R. & Masters, G., 1991b. Lower mantle structure from *ScS-S* differential travel times, *Nature,* **352,** 231–233.

Zhang, Z. & Lay, T., 1993. Investigation of upper mantle discontinuities near northwestern Pacific subduction zones using precursors to *sSH, J. geophys. Res.,* **98,** 4389–4405.

Zhao, L. & Chevrot, S., 2003. *SS*-wave sensitivity to upper mantle structure: Implications for the mapping of transition zone discontinuity topographies, *Geophys. Res. Lett.,* **30,** doi:10.1029/2003GL017223.

SUPPLEMENTARY MATERIAL

The following supplementary material is available for this article:

Appendix S1. In the supplementary appendix we evaluate time corrections (PDF format).

This material is available as part of the online article from: http:// www.blackwell-synergy.com/doi/abs/10.1111/j.1365-246X. 2008.03719.x
(this link will take you to the article abstract).

Please note: Blackwell Publishing are not responsibe for the content or functionality of any supplementary materials supplied by the authors. Any queries (other than missing material) should be directed to the corresponding author for the article.